BIOCHEMISTRY
including biophysical chemistry & molecular biology

Article

pubs.acs.org/biochemistry

Protein Dynamics and Ion Traffic in Bacterioferritin

Huan Rui,[†] Mario Rivera,*[,‡] and Wonpil Im*[,†]

[†]Department of Molecular Biosciences and Center for Bioinformatics and [‡]Department of Chemistry, The University of Kansas, Lawrence, Kansas 66047, United States

Supporting Information

ABSTRACT: Bacterioferritin (Bfr) is a spherical protein composed of 24 subunits and 12 heme molecules. Bfrs contribute to regulate iron homeostasis in bacteria by capturing soluble but potentially toxic Fe^{2+} and by compartmentalizing it in the form of a bioavailable ferric mineral inside the protein's hollow cavity. When iron is needed, Fe^{3+} is reduced and mobilized into the cytosol as Fe^{2+}. Hence, key to the function of Bfr is its ability to permeate iron ions in and out of its interior cavity, which is likely imparted by a flexible protein shell. To examine the conformational flexibility of Bfrs in a native-like environment and the way in which the protein shell interacts with monovalent cations, we have performed molecular dynamics (MD) simulations of BfrB from *Pseudomonas aeruginosa* (Pa BfrB) in K_2HPO_4 solutions at different ionic strengths. The results indicate the presence of coupled thermal fluctuations (dynamics) in the 4-fold pores and B-pores of the protein, which is key to allowing passage of monovalent cations through the protein shell using B-pores as conduits. The MD simulations also show that Pa BfrB ferroxidase centers are highly dynamic and permanently populated by transient cations exchanging with other cations in the interior cavity, as well as the solution bathing the protein. Taken together, the findings suggest that Fe^{2+} passes across the Pa BfrB shell via B-pores and that the ferroxidase pores allow the capture and oxidation of Fe^{2+}, followed by translocation of Fe^{3+} to the interior cavity, aided by the conformationally active H130.

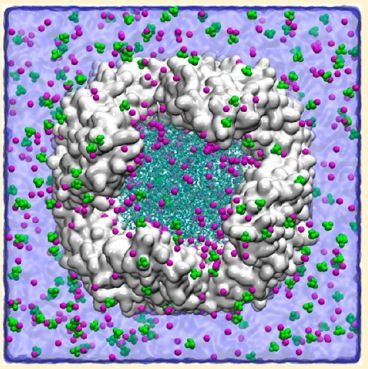

Iron is the fourth most abundant metal on Earth and an indispensable cofactor in the active sites of proteins and enzymes, where it functions as an integral component of physiological processes such as respiration, DNA synthesis, gene regulation, degradation of peroxides and superoxides, oxygen transport and oxygen activation, and degradation of xenobiotics.[1] Fe^{2+} is soluble (~0.1 M at pH 7.0) but readily oxidized by molecular oxygen to the Fe^{3+} form, which is extremely insoluble (~10^{-18} M at pH 7.0).[1,2] The oxidation of Fe^{2+} by O_2 generates hydrogen peroxide, which is also a byproduct of aerobic respiration; Fe^{3+} can be reduced to Fe^{2+} by reducing agents in the cell and rapidly react with hydrogen peroxide to produce Fe^{3+} and the hydroxyl radical, thus creating a cycle conducive to the formation of the highly reactive $^{\bullet}OH$, which indiscriminately attacks biological molecules.[2,3] Thus, the potential toxicity of Fe^{2+} and the insolubility of Fe^{3+} pose enormous challenges to living cells. These challenges have been largely ameliorated by evolution of the ferritins and ferritin-like molecules, which specialize in the handling and storage of iron. These molecules function by oxidizing the soluble but potentially toxic Fe^{2+} using O_2 or H_2O_2 as an electron acceptor and by storing the otherwise insoluble Fe^{3+} in the form of a mineral in a compartment (protein internal cavity) that is isolated from cellular processes. When necessary, iron stored in the internal cavities of ferritin-like molecules can be reduced, mobilized from the interior cavity, and incorporated into cellular processes.[1]

The crucial contribution of ferritin-like molecules to iron metabolism is evident in their presence in all three domains of life with remarkable conservation of structure in spite of very low levels of conservation in sequence.[4] Three types of ferritin-like molecules are found in bacteria, bacterioferritin (Bfr), ferritin (Ftn), and DNA binding proteins from starved cells (Dps).[1] Bfrs and Ftns are spherical proteins composed of 24 subunits that encase a hollow cavity approximately 80 Å in diameter where the iron mineral is stored. Dps are also spherical proteins but are composed of 12 subunits encasing a hollow cavity approximately 45 Å in diameter. Structures of Bfr from several organisms[5−11] reveal that the canonical fold of a Bfr subunit (Figure 1A) is composed of a four-helix bundle (helices A−D) and a short C-terminal helix E nearly perpendicular to the bundle. Each subunit harbors a ferroxidase center in which a di-Fe^{2+} moiety is oxidized to a di-Fe^{3+} species, prior to their storage as an iron mineral in the Bfr interior cavity. A unique property of the Bfrs, which exist only in archaea and bacteria,[4] is that they bind heme between two subunits (subunit dimer) (Figure 1B) such that the 24-mer protein consists of 12 subunit dimers and 12 heme molecules.

The protein shells of ferritin-like molecules function like cell membranes in that they separate the iron mineral from the cytosol. Four types of pores are thought to allow communication between the interior cavity of a 24-mer assembly with the exterior milieu: eight 3-fold pores (Figure 1C), six 4-fold pores (Figure 1D), a ferroxidase pore in each

Received: October 1, 2012
Revised: November 11, 2012
Published: November 21, 2012

   dx.doi.org/10.1021/bi3013388 | *Biochemistry* 2012, 51, 9900−9910

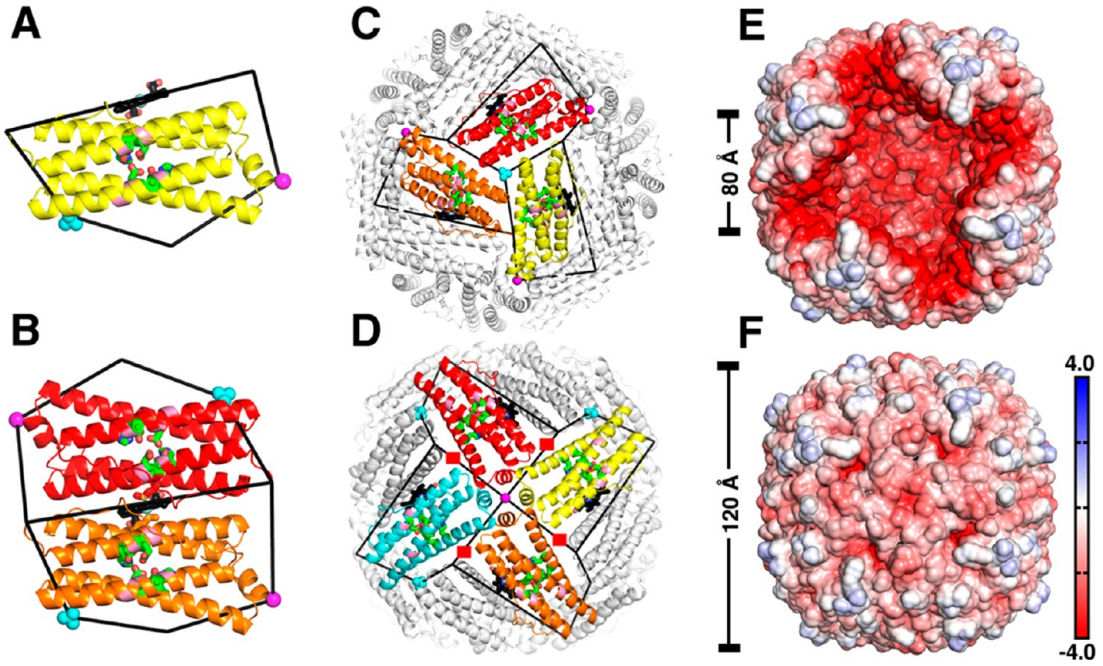

Figure 1. Bacterioferritin architecture. (A) View of a Pa BfrB subunit illustrating the ferroxidase center (green) and the ferroxidase pore (pink), which permits access of iron from the protein exterior to the ferroxidase center. Heme is colored black, and crystal K^+ in the 4-fold pore and PO_4^{3-} in the 3-fold pore are shown as magenta and cyan spheres, respectively. (B) Subunit dimer showing heme coordinated axially by a M52 from each subunit. (C) View along a 3-fold symmetry axis depicting a 3-fold pore and a phosphate ion. (D) View along a 4-fold symmetry axis illustrating a 4-fold pore and the associated K^+ ion. Each 4-fold pore is surrounded by four B-pores, highlighted by red squares. (E) Electrostatic potential mapped on the interior surface of Pa BfrB. The four front subunits were removed for a clear view of the internal cavity. (F) Electrostatic potential mapped on the exterior surface of a Pa BfrB with the same orientation as in panel E. Negative electrostatic potential is colored red and positive electrostatic potential blue, and the unit is kcal/mol/*e* where *e* is the unit charge. The figures were produced using the molecular visualization program PyMOL.[37]

subunit (Figure 1A), and four B-pores located near each of the 4-fold pores (Figure 1D).[11] Notably, the surface lining the interior cavity (interior surface) of Bfrs exhibits a very large negative potential (Figure 1E),[6,11] whereas the surface of the protein exposed to the protein exterior (exterior surface) shows less pronounced positive and negative electrostatic potentials (Figure 1F).

Structural studies showed that the 3-fold pores of eukaryotic ferritins are lined with conserved negatively charged residues. Substitution of these conserved residues caused decreased rates of iron uptake, leading to the suggestions that Fe^{2+} ions may move in and out of eukaryotic ferritins via 3-fold pores.[12−15] In comparison, the function of the 3-fold pores in the Bfrs, which are lined by layers of alternating positive and negative charge, is much less clear. Sulfate and phosphate ions have been observed in 3-fold pores in the crystal structures of *Pseudomonas aeruginosa* BfrB (Pa BfrB),[16] Pa FtnA,[17] and *Desulfovibrio desulfuricans* Bfr (Dd Bfr),[18] suggesting that in the Bfrs and bacterial Ftns the 3-fold pores may be conduits for anion traffic across the 24-mer shell. The 4-fold pores of Bfrs and bacterial Ftns are also structurally different from those of eukaryotic ferritins. The 4-fold pores in eukaryotic ferritins are lined by hydrophobic residues and are narrower than the 3-fold pores. In agreement, substantial barriers for the entry of Fe^{2+} and Na^+ ions into eukaryotic ferritin 4-fold pores have been calculated.[19] In contrast, the 4-fold pores of Bfrs typically contain hydrophilic residues and in some instances are observed to bind monovalent and divalent cations in X-ray crystal structures. The presence of these positively charged ions in the 4-fold pores of Bfrs has led to the hypothesis that these channels may serve as conduits for the traffic of Fe^{2+} into and out of the Bfr shell.[16,20,21] The protein shells of bacterial ferritins (Bfr and Ftn) also have channels at the intersection of three subunits, not aligned with any axis of symmetry in the structure. These channels have been termed B-pores.[18] In all known Bfr structures, the B-pores are lined by hydrophilic residues and have a relatively large number of negatively charged residues. Mg^{2+} ions coordinated by water molecules have been observed within the B-pores of *Azotobacter vinelandii* (Av)[21] and *Mycobacterium smegmatis* (Ms) Bfrs.[5] A more recent structure of Pa BfrB in complex with its cognate electron donor partner, Pa ferredoxin (Bfd), shows Na^+ ions in the B-pores, where they are coordinated by three negatively charged residues lining the narrowest section of the pores.[22] Although the function of the B-pores is unknown, it has been noted that B-pores are sufficiently large to accommodate a Fe^{2+} ion, thus suggesting that B-pores may function to facilitate trafficking of iron into and out of Bfrs and bacterial Ftns.

Clearly, the different pores in the ferritin structure are likely important for the dual function of iron uptake and release exhibited by ferritins and ferritin-like molecules. However, our current understanding of how the pores allow these functions is limited. Although the perception of ferritin-like molecules has evolved from that of a rigid cage to that of a dynamic supramolecular assembly, virtually nothing is known about their dynamic properties, and how dynamics allow their function. In an attempt to bridge these gaps, to the best of our knowledge, we report the first molecular dynamics (MD) simulation study of the 24-mer Pa BfrB. Results from these MD simulations reveal that significant cooperative dynamics at 4-fold pores and B-pores are linked to the traffic of K^+ ions across the protein shell, using B-pores as conduits. Moreover, the simulations

dx.doi.org/10.1021/bi3013388 | *Biochemistry* 2012, 51, 9900−9910

show highly dynamic ferroxidase centers permanently populated by transient K^+ ions, which can access the centers from the interior cavity as well as from the protein exterior. The traffic and distribution of K^+ observed during the simulations are discussed in the context of iron uptake and release from the Bfrs.

MATERIALS AND METHODS

Constructing the Pa BfrB System. The Pa BfrB structure used in the simulations [Protein Data Bank (PDB) entry 3ISF][6] was retrieved using the *PDB Reader* module in CHARMM-GUI (http://www.charmm-gui.org).[23] The terminal residues, including M1, D157, and D158, were missing in some of the Pa BfrB subunits. These residues were added using the IC BUILD command in CHARMM[24] and were patched with acetylated N-termini and *N*-methylamide C-termini, respectively. Because the MD simulations of Pa BfrB were conducted in a K_2HPO_4 solution (see below), PO_4^{3-} ions were added in the 3-fold pores in place of the SO_4^{2-} ions found in the crystal structure of the iron-soaked Pa BfrB structure (PDB entry 3IS8);[6] this structure was not used in the simulations because it was obtained from Pa BfrB containing ~600 iron atoms inside the central cavity.[6] Hence, the structure used in the simulations consists of a protein shell made of 24 Pa BfrB subunits, 12 heme molecules, K^+ in each of the six 4-fold pores, and PO_4^{3-} in each of the eight 3-fold pores (Figure 1A–D).

Estimating Initial Ion Positions from GCMC/BD Simulations. Having a proper starting system configuration for a MD simulation is extremely important. In the case of Pa BfrB, how to place the ions to initialize the MD simulations is the key issue, because Pa BfrB has a net charge of −378 and an uncorrelated system could take a long time to equilibrate. Under such a scenario, randomly placing the ions throughout a Pa BfrB may not be an optimal choice. Therefore, grand canonical Monte Carlo/Brownian dynamics (GCMC/BD) simulations were employed to generate the initial ion positions that follow the electrochemical potential in the system for the subsequent MD simulations.

The structure of Pa BfrB was centered in the origin of a cubic simulation box with 160 Å on each side. The vectors connecting two 4-fold pores on the opposite sides of the protein shell were aligned with the *X*-, *Y*-, and *Z*-axes. The CHARMM-GUI *GCMC/BD ion simulator* module[25] was employed to calculate the grid-based potential maps for the GCMC/BD simulations. The grid spacing was set to 0.5 Å. To account for the influence of different protein dielectric constants (ε_p) on the electrostatic potential, a series of ε_p values (2, 4, 10, 20, and 40) were used in the calculations, resulting in five sets of potential maps. They were denoted E2, E4, E10, E20, and E40, respectively. Each set contains electrostatic potential ϕ_{sf}, reaction field potential ϕ_{rf}, and core-repulsive steric potential U_{core}. From these, a space-dependent multi-ion potential of mean force, $\mathcal{W}(\{\mathbf{r}_i\})$, can be evaluated by

$$\mathcal{W}(\{\mathbf{r}_i\}) = \sum_i q_i[\phi_{sf}(\mathbf{r}_i) + \phi_{rf}(\{\mathbf{r}_i\})] + \sum_i U_{core}(\mathbf{r}_i) + \sum_i \sum_{j\neq i} U_{ij}(|\mathbf{r}_i - \mathbf{r}_j|) \quad (1)$$

where $\mathbf{r}_i$ is the position of the *i*th ion and U_{ij} denotes the pairwise ion–ion interactions.[26] $\mathcal{W}(\{\mathbf{r}_i\})$ is used to guide the GCMC/BD simulations following the BD equation of motion[27,28]

$$\frac{d\mathbf{r}_i}{dt} = -\frac{D_i}{k_B T}\cdot\frac{\partial \mathcal{W}(\{\mathbf{r}_i\})}{\partial \mathbf{r}_i} + \zeta(t) \quad (2)$$

with D_i and $\zeta(t)$ representing the diffusion constant of the *i*th ion and the stochastic water bombardment on ions, respectively.

Five GCMC/BD simulations (GCMC/BD_E2–E40) with 30000 steps each were performed using the last step input file from the *GCMC/BD ion simulator* module.[25] The positions of the protein atoms, heme molecules, and crystal ions in the pores were fixed. In each simulation, K^+ and Cl^- were added to the system from the GCMC buffer region equivalent in size to the simulation box and distributed by the subsequent BD simulations. K^+ instead of Fe^{2+} was used as the cation species in the GCMC/BD and the following MD simulations because of (i) the accessibility of accurate force field parameters for K^+ but not for Fe^{2+} and (ii) the similarity of K^+ and Fe^{2+} in that they are both soluble cations (see more discussion on the difference between K^+ and Fe^{2+} in Summary and Conclusions). The anion in the GCMC/BD simulations is Cl^-, which is different from the HPO_4^{2-} present in the MD simulations. This is because there are no accurate Lennard-Jones and short-range ion–ion interaction parameters for K_2HPO_4 available in GCMC/BD, but those parameters for KCl are well established and frequently used.[25,26] The total number of ions after each cycle was plotted for each system (Figure S1 of the Supporting Information). A snapshot of ion positions was selected after the ion number in each system reached a plateau value. To generate the initial ion configuration for the MD simulation systems, half of the Cl^- ions were randomly chosen and discarded, and the other half was replaced with HPO_4^{2-} to keep the total negative charge constant. Table 1 shows the number of ions in each system. Clearly, the resulting number of ions is strongly dependent on ε_p and increases with a decrease in ε_p. Instead of choosing a particular ε_p, we considered all systems with different ε_p values in this study to reflect the different ionic strengths.

Table 1. Numbers of K^+ ($N_{K\text{-total}}$), HPO_4^{2-} ($N_{phos\text{-total}}$), Cavity K^+ ($N_{K\text{-cavity}}$), and Cavity HPO_4^{2-} ($N_{phos\text{-cavity}}$) Ions, Water Molecules (N_{water}), and Total Atoms ($N_{atom\text{-total}}$) in the MD Simulation Systems

	$N_{K\text{-total}}$	$N_{phos\text{-total}}$	$N_{K\text{-cavity}}$	$N_{phos\text{-cavity}}$	N_{water}	$N_{atom\text{-total}}$
E2	2840	1231	1430	0	110172	404112
E4	1800	711	918	1	112343	406465
E10	1042	332	512	1	113992	408380
E20	788	205	334	2	114487	408849
E40	714	168	246	3	114478	408526

MD Simulations of Pa BfrB in K_2HPO_4 Solutions. In the preparation of the all-atom MD simulations, each of the five resulting systems from the GCMC/BD simulations (MD_E2–E40) was immersed in a pre-equilibrated water box of the same size as in the GCMC/BD systems (160 Å × 160 Å × 160 Å). Water molecules within 2.4 Å of the ions and the Pa BfrB heavy atoms were removed. The systems were then subjected to a 210 ps equilibration cycle with decreased positional harmonic restraints on heavy atoms excluding water oxygen. During the equilibration process, some water molecules infiltrated the Pa BfrB shell, creating vacuum pockets in the K_2HPO_4 solution

dx.doi.org/10.1021/bi3013388 | *Biochemistry* 2012, 51, 9900–9910

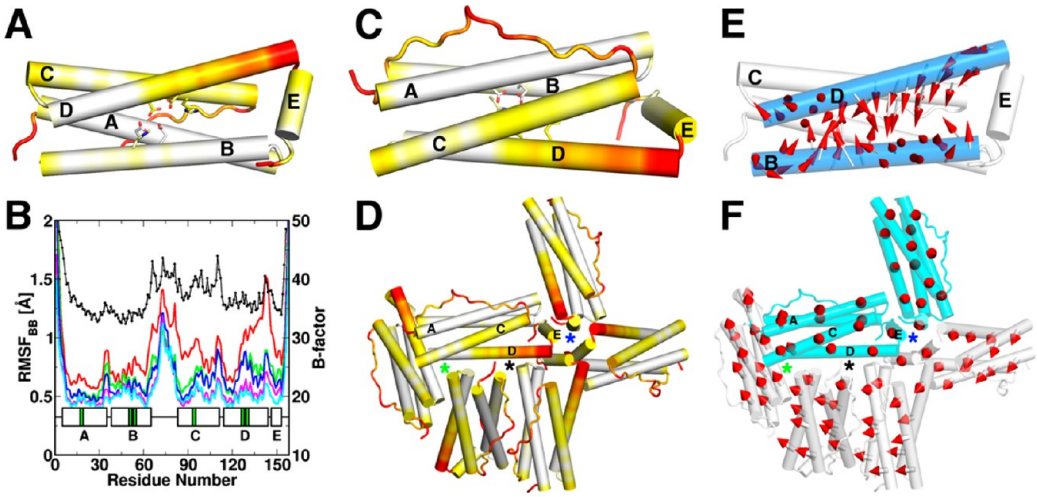

Figure 2. Intrinsic flexibility in Pa BfrB. The per-residue rmsf observed in system MD_E2 mapped onto a subunit viewed from the (A) interior and (C) exterior surface of Pa BfrB. Flexibility increases along the color scale from white to red. (B) Per-residue rmsf in a subunit of Pa BfrB plotted for systems MD_E2 (red), MD_E4 (green), MD_E10 (blue), MD_E20 (magenta), and MD_E40 (cyan). Per-residue *B* factors from the X-ray structure (PDB entry 3ISF) are shown in the black trace; helices A–E are indicated as boxes, and ferroxidase center residues are highlighted in green. (D) Per-residue rmsfs mapped on six subunits of the 24-mer assembly show relatively large dynamic behavior near 4-fold pores and B-pores, and considerably less dynamic activity near 3-fold pores. To facilitate visualization, the pores are highlighted by black (B-pores), green (3-fold pores), and blue (4-fold pores) stars. (E) Principal motional mode of C_α atoms on helices B and D (blue) in subunit H in MD_E40 shown by arrows. (F) Principal motional mode of six subunits of the 24-mer assembly shown in the same orientation as in panel D. The helices were segmented into 10-residue pieces, and the motions were calculated on the basis of the centers of mass of these structural segments. The arrows (red) indicate the directions of motion. Subunits exhibiting overall motion along and perpendicular to the assembly plane are colored white and cyan, respectively.

inside and outside of Pa BfrB. Therefore, the water molecules in the systems were removed after the first cycle of equilibration followed by addition of water in the manner described above except that 2.0 Å was used as a distance cutoff instead of 2.4 Å, and a second cycle of 780 ps equilibration was conducted. At the end of this cycle, small vacuum regions were still observed, but only in the central cavity. Therefore, a sphere of pre-equilibrated water with a radius of 40 Å was appended, and newly added water molecules within 2.4 Å of any heavy atoms in the system were deleted. The whole system was then equilibrated without restraints for 20 ps, which was followed by a 40 ns production. The system information is summarized in Table 1.

All the simulations were conducted in *NPT* ensembles using NAMD2.8[29] with the CHARMM all-atom parameter set PARAM22,[30] including the dihedral cross-term corrections (CMAP)[31] and a modified TIP3P water model.[32] The van der Waals interactions were smoothly switched off at 10–12 Å by a force switching function,[33] and the electrostatic interactions were calculated using the particle mesh Ewald method with a mesh size of ~1 Å. The temperature (300 K) and pressure (1 atm) were kept constant during all the simulations by Langevin dynamics and the hybrid Nose-Hoover Langevin piston method, respectively. The Langevin damping coefficient was set to 1 ps^{-1}; the decay period and damping time scale were 50 and 25 fs, respectively.

Principal Component Analysis. Principal component analysis (PCA) was performed to investigate the intrinsic dynamics of the Pa BfrB monomers and the assembly. Prior to calculating the covariance matrix for PCA, all the Pa BfrB structures were superimposed with the starting structure to remove the protein's translation and rotation during the simulations. For each of the Pa BfrB monomers, the coordinates of all the C_α atoms (**R**) were recorded at each trajectory snapshot

$$\mathbf{R} = \begin{bmatrix} r_{1,1} & r_{2,1} & r_{3,1} & \cdots & r_{3N-2,1} & r_{3N-1,1} & r_{3N,1} \\ r_{1,2} & r_{2,2} & r_{3,2} & \cdots & r_{3N-2,2} & r_{3N-1,2} & r_{3N,2} \\ \vdots & \vdots & \vdots & \ddots & \vdots & \vdots & \vdots \\ r_{1,T} & r_{2,T} & r_{3,T} & \cdots & r_{3N-2,T} & r_{3N-1,T} & r_{3N,T} \end{bmatrix} \quad (3)$$

where $r_{3n-2,t}$, $r_{3n-1,t}$, and $r_{3n,t}$ represent the *X*-, *Y*-, and *Z*-coordinates of the *n*th C_α atom at time *t*, respectively, and *N* (*N* = 158) is the total number of C_α atoms in a subunit. Using **R**, a covariance matrix (**Σ**) can be constructed

$$\mathbf{\Sigma} = \begin{bmatrix} \mathrm{cov}(r_1, r_1) & \mathrm{cov}(r_2, r_1) & \cdots & \mathrm{cov}(r_{3N}, r_1) \\ \mathrm{cov}(r_1, r_2) & \mathrm{cov}(r_2, r_2) & \cdots & \mathrm{cov}(r_{3N}, r_2) \\ \vdots & \vdots & \ddots & \vdots \\ \mathrm{cov}(r_1, r_{3N}) & \mathrm{cov}(r_2, r_{3N}) & \cdots & \mathrm{cov}(r_{3N}, r_{3N}) \end{bmatrix} \quad (4)$$

where the covariance of r_i and r_j, $\mathrm{cov}(r_i,r_j)$, over a total of *T* time points is defined by

$$\mathrm{cov}(r_i, r_j) = \frac{\sum_{t=1}^{T} (r_{i,t} - \overline{r}_i)(r_{j,t} - \overline{r}_j)}{T - 1} \quad (5)$$

where $\overline{r}_i$ and $\overline{r}_j$ are the time averages of all the $r_{i,t}$ and $r_{j,t}$ values, respectively. The eigenvalues and eigenvectors of the matrix **Σ** were computed. The eigenvector corresponding to the largest eigenvalue was then recorded and grouped into three groups for each C_α atom. The vector formed by these three values gives the principal direction of motion of a specific C_α atom.

The calculation of the principal motional modes of the entire Pa BfrB assembly is rooted in the same concept. Rather than using the coordinates of all the C_α atoms in the assembly, the center of mass coordinates of helical fragments were used. To distinguish motions occurring in different portions on helices A–D, each of them was divided into three fragments with each

dx.doi.org/10.1021/bi3013388 | *Biochemistry* 2012, 51, 9900–9910

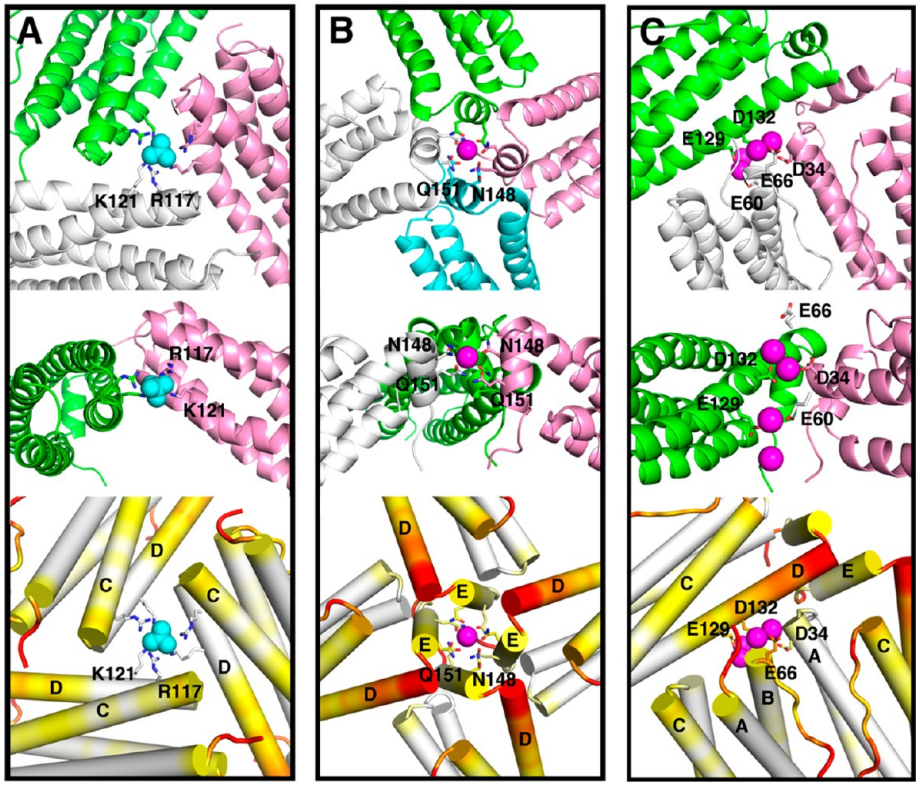

Figure 3. Architecture and dynamic properties of the pores in BfrB taken from a snapshot in system MD_E40: (A) 3-fold pores, (B) 4-fold pores, and (C) B-pores. Each pore type is shown viewed from the protein exterior (top) and from a transverse perspective (middle), with the internal cavity at the bottom and with the subunit closer to the viewer removed for the sake of clarity. The bottom panels show the intrinsic flexibility of each type of pore highlighted by mapping the rmsfs (see Figure 2D) from lowest (white) to highest (red). The phosphate ions in the 3-fold pores (cyan spheres) are coordinated by the side chains of R117 and K121 from each of the three subunits forming the pore. The K^+ ions (magenta spheres) in the 4-fold pores are coordinated by N148 and Q151 from each of the four E helices forming the pore. B-pores harbor negatively charged residues, including D34, E60, E66, D132, and E129. These residues attract K^+ ions and translocate them across the protein shell during the simulations.

one containing approximately 10 residues. Helix E contains only six residues, and thus, the entire helix was used. The center of mass coordinates of these helical fragments were recorded and used to construct the **R** matrix with an *N* of 13. The rest of the calculation followed the description given above.

RESULTS AND DISCUSSION

Structural Stability and Dynamics of Pa BfrB. The calculated backbone root-mean-squared deviation (rmsd) of Pa BfrB bathed in a K_2HPO_4 solution indicates that the protein is stable during the simulations (Table S1 of the Supporting Information). Even the systems with the most flexibility (E2 and E4) show rmsd values well under 4.0 Å. The greater rmsd in these systems likely stems from enhanced flexibility in specific regions of a Pa BfrB subunit, as can be seen in the per-residue rms fluctuations (rmsf) in Figure 2A–C. Nonetheless, the characteristic 432-point symmetry of the Bfr assembly is preserved during the simulations, which is a strong indicator that the integrity of the Pa BfrB structure is well maintained.

A per-residue rmsf plot (Figure 2B) illustrates the relative fluctuations in a Pa BfrB subunit for each of the MD systems (E2, E4, E10, E20, and E40). In addition to the N- and C-termini, it is apparent that specific regions of a subunit are significantly more dynamic than average. The relative extent of per-residue rmsf mapped onto a BfrB subunit is shown in panels A and C of Figure 2, with white representing the weakest propensity and red the strongest propensity to fluctuate. In addition to the N- and C-termini, the long loop connecting helices B and C (BC loop) and the C-terminus of helix D exhibit the strongest tendency to fluctuate, followed by the C-terminal half of helix D, and by the N-terminal half of helix C. The sections with higher than average flexibility also exhibit higher *B* factors than the rest of the subunit in the Pa BfrB crystal structure (black trace in Figure 2B). It is also interesting that the mobility of these regions increases with the increase in K_2HPO_4 concentration (Figure 2B). Nevertheless, analyses of the principal motional modes of C_α atoms reveal the absence of correlated motions within each of the helices and among different helices in a subunit (Figure 2E).

Although no clear functional implications can be derived from fluctuations within an individual subunit, their significance emerges in the context of the 24-mer assembly. This is illustrated in Figure 2D by a minimal assembly of six Pa BfrB subunits containing a 3-fold pore (green star), a 4-fold pore (blue star), and a B-pore (black star). Clearly, the regions that exhibit increased mobility in each of the subunits constitute the pores in the Bfr structure. This is particularly evident in the area surrounding the 4-fold pores, including the B-pores. In comparison, the regions comprising the 3-fold pores have much less dynamical activity. These observations suggest that while the less mobile sections of a Pa BfrB subunit may be important for maintaining the structural integrity of the four-helix bundle and the 24-mer assembly, the fluctuations of high-mobility residues impart the dynamic behavior to the pores in the Bfr shell. This aspect is further elaborated below after some salient points regarding each of the pores have been addressed.

dx.doi.org/10.1021/bi3013388 | *Biochemistry* 2012, 51, 9900–9910

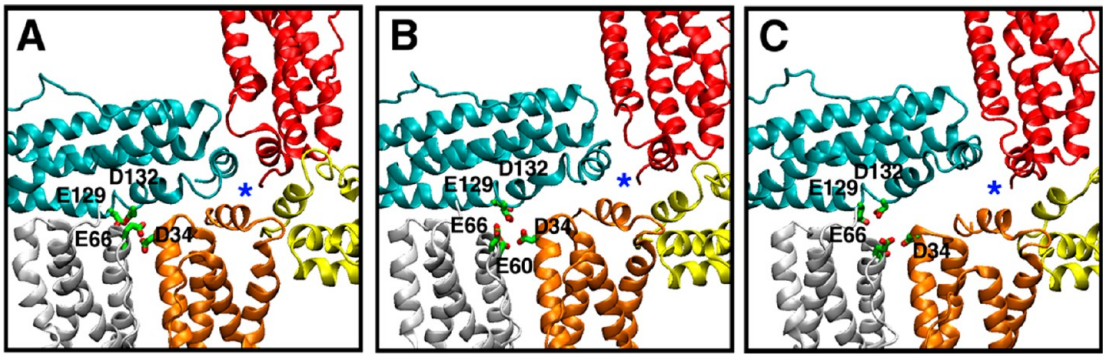

Figure 4. Snapshots illustrating the dynamic behavior of the 4-fold pores and B-pores. (A) A 4-fold pore (blue star) and one of its surrounding B-pores highlighted by its negatively charged residues (green), as seen in the crystal structure. (B) Melting of the C-terminal sections of the D helices (Figure 2C) opens the B-pore and increases the mobility of the entire E helix in the cyan subunit. This marks the start of 4-fold pore deformation. (C) Helix E in the cyan subunit moves farther from its neighboring E helix (orange) toward the D helix in the same subunit, which is now refolded. The displacement of helix E results in deformation of the 4-fold pore and the further expansion of the B-pore. All the structure snapshots were taken along the MD_E2 trajectory.

In addition to the fluctuation of residues near the pores, neighboring subunits can also adjust their orientations relative to one another, effectively creating breathing motions in the 24-mer protein. Figure 2F illustrates the principal motional modes of subunits within the minimal Pa BfrB assembly that includes each of the 3-fold pores, 4-fold pores, and B-pores. Motions of subunits that are in the immediate vicinity are usually coupled (share similar directionality), although in some cases adjacent subunits may move in orthogonal directions.

The 3-fold pore, 4-fold pore, and B-pore conformations are mostly maintained during the simulations. As shown in Figure 3A, the 3-fold pore is lined by three subunits; specifically, the C-terminus of helix C forms the outermost layer of the pore, while the N-terminus of helix D forms the innermost layer. Near its narrowest section, there is a PO_4^{3-} replacing the SO_4^{2-} observed in the crystal structure (see Materials and Methods). During the course of the simulations, the PO_4^{3-} is always coordinated by the side chains of R117 and K121 (Figure 3A) and does not exit the 3-fold pores. As shown in Figure 3B, a 4-fold pore is formed by four E helices adopting an orientation that is more or less parallel to the pore axis. The BfrB crystal structure contains a K^+ ion in each 4-fold pore where it is coordinated by the side chains of N148 and Q151. During the simulations, many of these K^+ ions stay inside the 4-fold pores as in the crystal structure (Figure 3B). In some cases, however, K^+ ions exit the pore. When this happens, the side chains of N148 and Q151 in E helices located on opposite sides of the pore interact, leading to temporary obstruction of the 4-fold pore. Unlike 3-fold or 4-fold pores, B-pores are not at a crystallographic axis of symmetry. As shown in Figure 3C, the side chains of D34, E60, E66, D132, and E129 in BfrB protrude into the pore interior, thus creating the narrowest section of the B-pores. In the course of all simulations, K^+ ions traverse B-pores aided by transient coordinative interactions with these negatively charged residues (Figure 3C). The fashion in which K^+ ions move through B-pores in our simulations is in agreement with recent experimental observations showing that Na^+ ions are coordinated by D34 from one subunit and by D132 and T136 from another subunit in the B-pores of Pa BfrB in complex with its cognate electron transfer partner Pa Bfd.[22] Along the same vein, Mg^{2+} ions have also been observed within the B-pores of Av BfrB[21] and Ms BfrB,[5] where they are coordinated by water molecules. These observations taken together strongly suggest that B-pores are conduits for the movement of ions into and out of the Pa BfrB central cavity.

The bottom row in Figure 3 clearly illustrates that 3-fold pores show modest dynamic behavior. In contrast, a significant concentration of fluctuating domains is observed in the external perimeter of 4-fold pores, extending toward B-pores. Key residues contributing to the enhanced dynamics observed in these regions are located in the C-terminus of helix D and the loop connecting helices D and E, specifically, residues Q137–G145. Moreover, in high-ion concentration systems (e.g., MD_E2), the C-termini of helices D undergo frequent transitions between folded and unfolded states; Figure 4 and Movie S1 of the Supporting Information document this transition and its impact on a 4-fold pore and one of its surrounding B-pores. The unfolding events in the D helices enhance the mobility of the entire E helices: one pair of diagonally opposed E helices comes close to one another, while the other pair is separated further. When the C-termini of the D helices refold, the corresponding E helices return to their original positions. In extreme cases, the folding and unfolding events yield a ratio of up to 0.58 for the distance between two diagonally opposed E helices in the proximity of each other relative to the distance separating two E helices moved farther apart (Figure 4B,C). Despite their dynamic nature, the 4-fold pores are mostly closed during the simulations as the deformation caused by their dynamics always places two E helices in close contact. The folding–unfolding events of the C-terminal portions of helices D affect the conformation of B-pores as well. Unfolding of the C-termini in the D helices expands the passageway across the B-pores (Figure 4B), while refolding either returns the pore to its initial closed state (Figure 4A) or keeps the pore open by deforming the nearby 4-fold pore (Figure 4C). The dynamic opening and narrowing of B-pores support the notion that ions move across the Pa BfrB shell using B-pores as conduits. Further evidence will be provided in the following section where the analysis of the ion distribution and motions is presented.

Ion Distributions in the Pa BfrB Systems. Although the interior surface of the protein shell exhibits a relatively large negative electrostatic potential (Figure 1E), the highest concentrations of negatively charged residues occur in the middle of each subunit near the ferroxidase center and in the perimeters surrounding 3-fold pores, 4-fold pores, and B-pores.

dx.doi.org/10.1021/bi3013388 | *Biochemistry* 2012, 51, 9900–9910

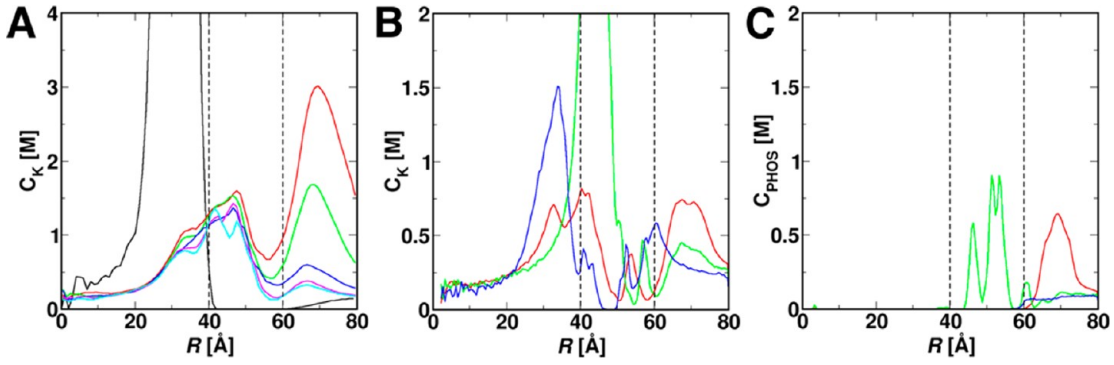

Figure 5. Potassium and phosphate ion concentration profiles (C_K and C_{PHOS}, respectively). C_K in panel A was calculated along the radial distance (R) from the center of the interior cavity with a bin size of 0.5 Å. The results for systems MD_E2 (red), MD_E4 (green), MD_E10 (blue), MD_E20 (magenta), MD_E40 (cyan), and GCMC/BD_E10 (black) are shown. To calculate C_K and C_{PHOS} in panels B and C, a cone is constructed with the apex at the center of BfrB interior cavity and axis collinear with the pore axis. The volume enclosed by the cone is then divided into 0.5 Å slabs along its axis, and concentrations of K^+ and phosphate ions are computed inside each slab. Results are shown for the 3-fold pores (green), 4-fold pores (blue), and B-pores (red) in MD_E10. The approximate positions of the inner and outer protein surfaces along R are indicated by the dashed black lines.

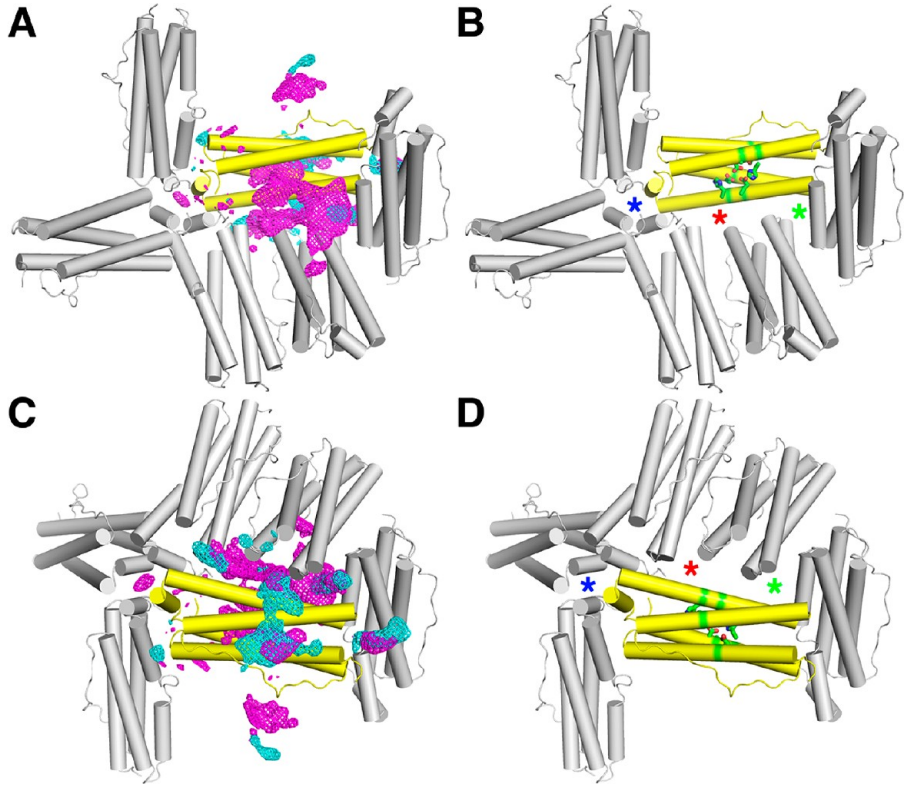

Figure 6. Potassium ions concentrated near pores in BfrB are in dynamic exchange. (A) Representative density of K^+ (magenta mesh) and HPO_4^{2-} (cyan mesh) in a minimal portion of the Pa BfrB assembly bearing a 3-fold pore, a 4-fold pore, and a B-pore viewed from the interior cavity. An identical view devoid of ion density is shown in panel B to facilitate identification of the 3-fold pores, 4-fold pores, and B-pores, which are highlighted by green, blue, and red stars, respectively. This view also shows the ferroxidase center residues (green) of subunit A (yellow). The views in panels C and D are from the exterior of the protein.

Because of the significant electrostatic potential gradients created by these residues, during the simulations, K^+ ions migrate toward the interior surface of BfrB and penetrate into the protein shell (black dashed lines in Figure 5) even though the majority of them stayed away from the protein shell in the GCMC/BD simulations with rigid BfrB (black line in Figure 5A). This is evident in Figure 5A, which plots the potassium ion concentration (C_K) along the radial distance (R) from the center of the interior cavity for systems GCMC/BD_E10 (black) and MD_E2-E40. Clearly, systems with different ionic strengths share similar profiles of C_K, strongly suggesting that the ion distribution has reached a steady state in all the systems and that the concentration profiles represent the real likelihood of having ions in different regions in a given system.

In particular, K^+ is concentrated near the 3-fold pores, 4-fold pores, and B-pores. This is clearly shown in the C_K profiles along the axes of the 3-fold pores, 4-fold pores, and B-pores in Figure 5B. The peaks observed in the profiles at R values of 32,

dx.doi.org/10.1021/bi3013388 | *Biochemistry* 2012, 51, 9900−9910

43, and 48 Å denote accumulation of K^+ near 4-fold pores, B-pores, and 3-fold pores, respectively. The accumulation of K^+ near the three types of pores can be viewed from the protein interior (Figure 6A) and exterior (Figure 6C), where the K^+ density is rendered as magenta mesh and the HPO_4^{2-} density as cyan mesh. Figure 6A also shows that the regions with high C_K values, especially those near the 3-fold pores, B-pores, and ferroxidase centers that are connected by bridges with lower C_K values. Importantly, in all simulations, there is a dynamic flow that exchanges ions between these "reservoirs"; Movie S2 of the Supporting Information shows individual ion trajectories visiting these reservoirs. There is also occasional exchange of K^+ between the 4-fold pore and the rest of the reservoirs.

In the context of the observations described above, the significance of a network of negative potential on the inner surface of Pa BfrB is that it provides routes for cations to move along the interior surface. It is therefore plausible that Fe^{3+} ions exiting the ferroxidase center into the interior cavity[6,10,11] move along the interior to the nucleation sites in a similar fashion. Similarly, Fe^{2+} that enters the cavity via B-pores may be efficiently transported to a ferroxidase center where it is oxidized to Fe^{3+} and subsequently transported to a nucleation site.

Unlike K^+ ions, which localize mainly within the subunit four-helix bundles or at the interior surface of BfrB, HPO_4^{2-} ions usually remain associated with the protein exterior surface, near the ferroxidase and B-pores (Figure 6C). As indicated above, the phosphate ions present within the 3-fold pores remain in their positions throughout the simulations (Figure 5C). The fact that not many HPO_4^{2-} ions are inside the central cavity is probably the result of the initial placement of these anions. Because the electrostatic potential inside the cavity is very negative (Figure 1E), HPO_4^{2-} ions are located predominantly in the solution bathing the protein exterior at the start of the simulations (Table 1). A few phosphate ions move fairly close to the protein during the simulations, especially in regions near the outermost layer of the B-pores. In systems with the highest HPO_4^{2-} concentration (MD_E2), the anion can co-appear with K^+ in the outer layer of the B-pores, but unlike K^+ ions, the anions do not penetrate the B-pores. Given the predominantly negative potential within the B-pores, it is unlikely that phosphate ions use this conduit to move across Pa BfrB. It is tempting to speculate that phosphate ions utilize 3-fold pores and there are two plausible reasons why this traffic is not observed in the simulations. First, the time scale of the simulation is short. Second, the possibility exists that access of phosphate to the interior cavity is promoted by the presence of iron concentrations within the cavity. As iron accumulates in the cavity, the positive charge carried by iron ions compensates for and eventually exceeds the negative potential created by the negatively charged Pa BfrB interior surface, thus allowing the entrance of phosphate, which is incorporated into the ferric mineral.

Ion Trafficking and Its Relation to Pa BfrB Dynamics. The simulations suggest that K^+ moves into and out of Pa BfrB exclusively through the B-pores (Table 2 and Movies S3 and S4 of the Supporting Information). The path traveled by K^+ across a B-pore consists of a series of negatively charged residues: E66 at the outermost layer, D34 and D132 in the middle, and E60 and E129 in the interior opening (Figure 3C). Among these residues, D34 and D132 are also found to coordinate Na^+ in the crystal structure of Pa BfrB in complex with Pa Bfd.[22] In the crystal structure of Av BfrB, three of these residues (D34, E66, and D132) and two additional ones (E135 and D139) are probably responsible for the presence of the Mg^{2+} ions inside the B-pores.[21] Considering the ability of these negatively charged residues to attract cations into the B-pores and further transport them across the protein shell, it is reasonable to suggest that Fe^{2+} ions enter and/or exit the BfrB central cavity via B-pores.

Table 2. Numbers of K^+ Ions Escaped ($N_{escaped}$) or Entered ($N_{entered}$) via the B-Pores during the 40 ns Trajectories in Systems MD_E2−E40

	E2	E4	E10	E20	E40
$N_{escaped}$	63	56	63	23	0
$N_{entered}$	5	2	4	3	4

The net number of K^+ ions moving out of the protein cage displays a slight dependence on the initial C_K inside the Pa BfrB cage. In general, a higher interior C_K results in more K^+ exiting the interior cavity, which is in agreement with the intuitive notion that K^+ flux occurs in response to concentration gradients across the protein shell. Also in agreement with the idea of flux controlled by a chemical potential is the observation that the total numbers of K^+ ions released in systems MD_E2, MD_E4, and MD_E10 in the 40 ns duration are not significantly different because the C_K in the external solution is high and comparable to the concentration of K^+ in the interior.

Communication between the Ferroxidase Center and the K_2HPO_4 Solution. The ferroxidase centers communicate with the K_2HPO_4 solution by allowing K^+ to enter from either the exterior or the interior K_2HPO_4 solution. At the beginning of the simulations, all the ferroxidase centers were devoid of cations. As the simulations proceed, there is one incidence of K^+ penetrating into a ferroxidase center from the external K_2HPO_4 solution via the previously identified ferroxidase pore.[6] The low frequency of this occurrence is probably linked to the fact that K^+ entering the protein from the exterior solution has to work against the concentration gradient. K^+ enters the pore steered by one of the ferroxidase center residues, E94, and reaches a pocket within the four-helix bundle, which is adjacent to the ferroxidase center and harbors two negatively charged residues, E44 and D90. Movie S5 of the Supporting Information documents this entering event. These observations are in agreement with the notion derived from X-ray crystallographic and kinetic studies in solution that the ferroxidase pores in Pa BfrB serve as ports for the entry of iron into the ferroxidase center.[6]

In the simulations, K^+ ions enter the ferroxidase centers from the interior K_2HPO_4 solution with a much higher frequency (Movie S6 of the Supporting Information). The events follow a well-defined path composed of several negatively charged residues (E47, D50, and E129) on helices B and D near the inner opening of the ferroxidase centers. Permeation of K^+ into the ferroxidase center from the interior cavity creates a unique organization of cations in and around the ferroxidase centers as depicted in Figure 7. Four sites are favored by K^+: two of them (① and ②) are close to the previously identified ferroxidase iron binding sites, the third (③) is near the exterior surface, and the fourth (④) is located adjacent to the ferroxidase center in the pocket created by E44 and D90, close to H130. The observation that cations such as K^+ are stabilized within the apo-ferroxidase centers is in line with the crystal structure of Pa FtnA, where Na^+ ions were found in the ferroxidase centers.[17]

dx.doi.org/10.1021/bi3013388 | Biochemistry 2012, 51, 9900−9910

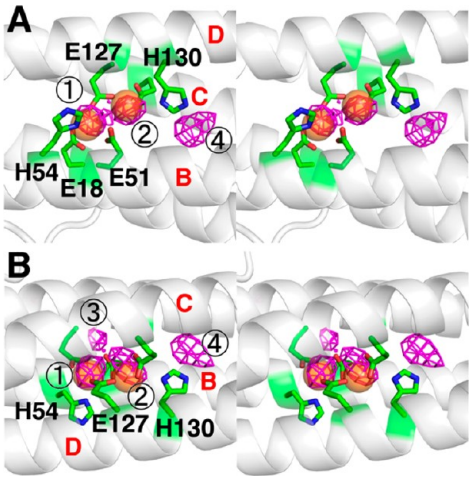

Figure 7. Potassium ions exchange in and out of ferroxidase centers. Stereoviews show the distribution of potassium ions (magenta mesh) close to the ferroxidase ligands (green) viewed from (A) the interior cavity of BfrB with helices B and D in the front and (B) the side of the subunit with helices C and D in the front. In panel B, the interior cavity is at the bottom and the protein exterior at the top. Panels A and B are related by a 90° rotation along the horizontal axis. Iron ions in the ferroxidase center of Pa BfrB (PDB entry 3IS8) are shown as orange spheres. Different helices are indicated by red letters.

In this context, the presence of K^+ within the ferroxidase centers not only is expected but also provides an important correlation to experimental observations that largely validate our approach and additional insights derived from the MD simulations.

Although sites ①–④ are always observed with K^+ bound, these K^+ ions do not necessarily remain at these sites during the entire course of the simulations. Rather, they exchange sites, predominantly between sites ② and ④. K^+ at site ② can also be released and replaced by another K^+ coming in from the interior cavity. The dynamic reorganization of K^+ in and around the ferroxidase centers is likely facilitated by H130 side chains. Two dominant side chain conformations of H130 are detected in all the simulations, with χ_1 angles of −180° and −60° (Figure 8) that correspond to the "gate-closed" and "gate-open" conformations, respectively, in the crystal structures of Pa BfrB obtained with and without iron in the ferroxidase center.[6] The transition between these two conformations swings the imidazole ring of H130 and disrupts interactions between K^+ and the ferroxidase center residues at the K^+ binding sites, especially site ②, which harbors the K^+ that exchanges frequently with the K_2HPO_4 solution in the interior cavity. Movie S6 of the Supporting Information exhibits the trajectory of a K^+ ion getting into site ② from the internal K_2HPO_4 solution assisted by H130 side chain motion.

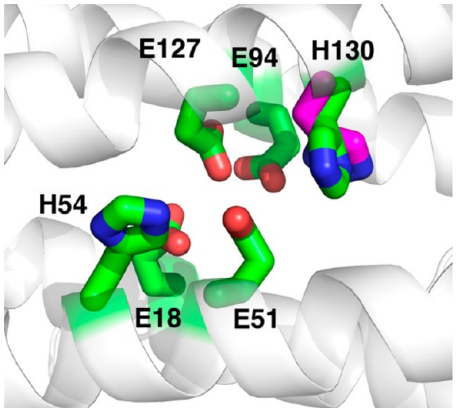

Figure 8. H130 in its gate-closed (magenta) and gate-open (green) conformations. For a clear view, K^+ ions are not included.

These observations taken together provide unique insights into the influence exerted by dynamics on the function of the ferroxidase centers in Pa BfrB. Cations such as K^+ and Na^+ are likely ubiquitously present in the ferroxidase centers, to which they gain access from either side of the protein shell. The monovalent ions flow in and out of the ferroxidase centers in large part aided by the dynamic pedaling of the H130 side chain. In this context, the translocation of K^+ from the ferroxidase center to the interior cavity observed during the simulations, which is gated by the conformational exchange of the H130 side chain, is reminiscent of the mechanism proposed for gating Fe^{3+} from the ferroxidase center to the interior cavity.[6] Hence, the MD simulations lend support to the gating role played by the side chain of H130 and provide unprecedented insight into the protein motions that allow cations to move through ferroxidase centers.

SUMMARY AND CONCLUSIONS

Bacterioferritin (Bfr) regulates cytosolic iron concentrations by oxidizing Fe^{2+} ions, compartmentalizing the Fe^{3+} as a mineral in its interior, and when necessary releasing Fe^{2+} into the cytosol for incorporation in metabolism. Hence, the Bfr shell separates the iron mineral from the cytosolic environment and protects it from indiscriminate reduction by reducing agents in the cell. To function as effective regulators of cytosolic iron concentrations, Bfrs must allow the efficient and directional flow of iron, either into their cavity (iron uptake) or out to the cytosol (iron mobilization). In the process of iron uptake, Fe^{2+} is thought to access the ferroxidase centers via ferroxidase pores and bind to ferroxidase center ligands to form di-Fe^{2+} complexes. These are subsequently oxidized to di-Fe^{3+} moieties, which are then translocated from the ferroxidase centers to the interior cavity, where the iron mineral is formed. Structural and kinetic studies conducted with Pa BfrB[6] have shown that H130, a ferroxidase center ligand, coordinates iron when its side chain is in a gate-closed conformation; a change to its gate-open conformation allows Fe^{3+} to move from the ferroxidase center to the interior cavity. Hence, the ferroxidase center of Pa BfrB is thought to function in the dual capacity of both a pore and a catalytic site.[6] In comparison, kinetic and structural studies with *E. coli* Bfr (Ec Bfr) showed that iron bound to the ferroxidase centers of Ec Bfr is not translocated into the interior cavity but functions as a cofactor that catalyzes the oxidation of Fe^{2+} that gained access to the interior cavity via a yet unknown type of pore (3-fold pore, 4-fold pore, or B-pore) in its structure.[8,35]

The current MD simulations are performed in K_2HPO_4 solutions. Although K^+ and Fe^{2+} are different in many ways, they share a certain degree of similarity. Both ions are soluble and carry positive charges. We suggest that the results obtained for K^+ in our simulations may be indicative of the behavior of Fe^{2+} as it moves in and out of the Bfr molecule. Clearly, the rich redox chemistry of iron (Fe^{2+}/Fe^{3+}) cannot be replicated using K^+. Nevertheless, the traffic of K^+ ions across the Bfr structure observed in our simulations either is in agreement with prior experimental observations or adds new insights, such as the traffic of K^+ through B-pores.

dx.doi.org/10.1021/bi3013388 | *Biochemistry* 2012, 51, 9900–9910

The simulation results reveal dynamically active ferroxidase centers (devoid of iron) in Pa BfrB, which are readily accessed by K^+ ions from the solution bathing the 24-mer, or from the interior cavity. In the simulations, K^+ in the external solution is seen to enter the ferroxidase center through the ferroxidase pore (Movie S5 of the Supporting Information), an observation that is in agreement with prior structural reports suggesting that as part of the iron uptake process Fe^{2+} ions access the ferroxidase center via ferroxidase pores.[6,11] The MD simulations also reveal that K^+ in the ferroxidase centers is in dynamic exchange with K^+ in the interior cavity (Movie S6 of the Supporting Information). Access of K^+ to and exit of K^+ from ferroxidase centers are facilitated by the dynamic behavior of the H130 side chain (Figure 8 and Movie S6 of the Supporting Information), which is seen to periodically alternate between a conformation similar to the iron-bound (gate-closed) state in the iron-bound BfrB crystal structure and a conformation similar to the iron-free (gate-open) state in the crystal structure of iron-free BfrB.[6] Consequently, the dynamic nature of the ferroxidase centers in Pa BfrB is reflected correctly in the MD simulations. The differences in the iron uptake process observed for Pa and Ec Bfr, despite their nearly identical structures, cannot be explained by the available data. Nevertheless, future efforts aiming at understanding the source of the differences are likely to provide important additional insights that will illuminate the details of how bacteria regulate cytosolic iron concentrations.

The recovery of Fe^{2+} from the Bfr cavity (iron mobilization) requires specific protein−protein interactions that allow the transfer of an electron from the [2Fe-2S] cluster of Bfr-associated Bfd to the iron mineral in Bfr.[22,36] Although Fe^{2+} is thought to exit the protein via pores in the structure, the type of pore used as a conduit is unknown. Crystal structures of Bfrs typically exhibit monovalent or divalent cations in the 4-fold pores, which has led to the suggestion that Fe^{2+} may utilize 4-fold pores to move across the Bfr protein shell. The MD simulations show that K^+ ions do not cross the Pa BfrB shell via 4-fold pores. Instead, K^+ ions traverse the BfrB shell using B-pores, assisted by conserved negatively charged residues (Movies S3 and S4 of the Supporting Information). The simulations also suggest that K^+ traffic through B-pores is allowed by folding−unfolding fluctuations in the C-termini of the D helices, which cause the B-pores to expand and contract (Figure 4 and Movie S1 of the Supporting Information). The folding−unfolding fluctuations of the D helices also cause lateral displacement of the E helices, placing two opposing E helices closer to each other while the other two are further separated (Figure 4 and Movie S1 of the Supporting Information). Such displacement of the E helices has the effect of narrowing the 4-fold pores. This not only causes some of the K^+ ions to exit the pores early in the simulations but also prevents ion traffic through them. It is important to note that the folding−unfolding fluctuations in the C-termini of the D helices are facilitated by the architecture of the 4-fold pores, which absorb the lateral translation of E helices with minimal perturbation to the 24-mer assembly. Hence, the coordinated fluctuations in and around 4-fold pores allow the B-pores to undergo "breathing" motions that allow the movement of ions through the Bfr shell. In this context, it is noteworthy that B-pores are not present in the structures of eukaryotic ferritins, where ion traffic is thought to occur through 3-fold pores.

■ ASSOCIATED CONTENT

Ⓢ Supporting Information

The rmsds of Pa BfrB in the MD simulations (Table S1), numbers of ions during the GCMC/BD simulations (Figure S1), the folding−unfolding transition of the C-terminal region of helix D and its impact on the 4-fold pores and B-pores (Movie S1), K^+ ion exchange between K^+ density reservoirs at the 3-fold pore, the B-pore, and the ferroxidase center (Movie S2), K^+ escaping the Pa BfrB cage from the B-pores (Movie S3), K^+ entering the central cavity using the B-pores (Movie S4), K^+ entering the ferroxidase center via the ferroxidase pore (Movie S5), and K^+ entering the ferroxidase center from the central cavity aided by the change in H130 side chain orientation (Movie S6). This material is available free of charge via the Internet at http://pubs.acs.org.

■ AUTHOR INFORMATION

Corresponding Author

*M.R.: Department of Chemistry, University of Kansas, 2030 Becker Dr., Lawrence, KS 66047; e-mail, mrivera@ku.edu; phone, (785) 864-4936. W.I.: Center for Bioinformatics and Department of Molecular Biosciences, University of Kansas, 2030 Becker Dr., Lawrence, KS 66047; e-mail, wonpil@ku.edu; phone, (785) 864-1993.

Funding

This work was supported by National Science Foundation Grant MCB-0918374 and MCB-1157677 (to W.I.), National Institutes of Health Grant R01-GM092950 (to W.I.), TeraGrid/XSEDE resources (Grant TG-MCB070009 to W.I.), and National Science Foundation Grant MCB-1158469 (to M.R.).

Notes

The authors declare no competing financial interest.

■ REFERENCES

(1) Andrews, S. C., Robinson, A. K., and Rodríguez-Quiñones, F. (2003) Bacterial Iron Homeostasis. *FEMS Microbiol. Rev. 27*, 215−237.

(2) Touati, D. (2000) Iron and oxidative stress in bacteria. *Arch. Biochem. Biophys. 373*, 1−6.

(3) Lewin, A., Moore, G. R., and Le Brun, N. E. (2005) Formation of protein-coated iron minerals. *Dalton Trans. 22*, 3597−3610.

(4) Andrews, S. C. (2010) The Ferritin-like Superfamily: Evolution of the Biological Iron Storeman from a Ruberythrin-like Ancestor. *Biochim. Biophys. Acta 1800*, 691−705.

(5) Janowski, R., Auerbach-Nevo, T., and Weiss, M. S. (2008) Bacterioferritin from *Mycobacterium smegmatis* contains zinc in its di-nuclear site. *Protein Sci. 17*, 1138−1150.

(6) Weeratunga, S. K., Lovell, S., Yao, H. L., Battaile, K. P., Fischer, C. J., Gee, C. E., and Rivera, M. (2010) Structural Studies of Bacterioferritin B from *Pseudomonas aeruginosa* Suggest a Gating Mechanism for Iron Uptake via the Ferroxidase Center. *Biochemistry 49*, 1160−1175.

(7) Cobessi, D., Huang, L. S., Ban, M., Pon, N. G., Daldal, F., and Berry, E. A. (2002) The 2.6 Å resolution structure of *Rhodobacter capsulatus* bacterioferritin with metal-free dinuclear site and heme iron in a crystallographic 'special position'. *Acta Crystallogr. D58*, 29−38.

(8) Crow, A., Lawson, T. L., Lewin, A., Moore, G. R., and Le Brun, N. E. (2009) Structural basis for iron mineralization by bacterioferritin. *J. Am. Chem. Soc. 131*, 6808−6813.

(9) Frolow, F., Kalb, A. J., and Yariv, J. (1994) Structure of a unique two-fold symmetric haem-binding site. *Nat. Struct. Biol. 1*, 453−460.

(10) Liu, H. L., Zhou, H. N., Xing, W. M., Zhao, J. F., Li, S. X., Huang, J. F., and Bi, R. C. (2004) 2.6 Å resolution crystal structure of the bacterioferritin from *Azotobacter vinelandii*. *FEBS Lett. 573*, 93−98.

(11) Macedo, S., Romao, C. V., Mitchell, E., Matias, P. M., Liu, M. Y., Xavier, A. V., LeGall, J., Teixeira, M., Lindley, P., and Carrondo, M. A. (2003) The nature of the di-iron site in the bacterioferritin from *Desulfovibrio desulfuricans*. *Nat. Struct. Biol. 10*, 285−290.
(12) Levi, S., Santambrogio, P., Corsi, B., Cozzi, A., and Arosio, P. (1996) Evidence that Residues Exposed on the Three-Fold Channels Have Active Roles in the Mechanism of Ferritin Iron Incorporation. *Biochem. J. 317*, 467−473.
(13) Treffry, A., Bauminger, E. R., Hechel, D., Hodson, N. W., Nowik, I., Yewdall, S. J., and Harrison, P. M. (1993) Defining the Roles of the Three-fold Channels in Iron Uptake, Iron Oxidation and Iron-Core Formation in Ferritin: A Study Aided by Site-Directed Mutagenesis. *Biochem. J. 296*, 721−728.
(14) Tosha, T., Behera, R. K., Ng, H. L., Bhattasali, O., Alber, T., and Theil, E. C. (2012) Ferritin Protein Nanocage Ion Channels: Gating by N-Terminal Extensions. *J. Biol. Chem. 287*, 13016−13025.
(15) Hempstead, P. D., Yewdall, S. J., Fernie, A. R., Lawson, D. M., Artymiuk, P. J., Rice, D. W., Ford, G. C., and Harrison, P. M. (1997) Comparison of the three-dimensional structures of recombinant human H and horse L ferritins at high resolution. *J. Mol. Biol. 268*, 424−448.
(16) Weeratunga, S., Lovell, S., Yao, H., Battaile, K. P., Fischer, C. J., Gee, C. E., and Rivera, M. (2010) Structural Studies of Bacterioferritin B (BfrB) from *Pseudomonas aeruginosa* Suggest a Gating Mechanism for Iron Uptake via the Ferroxidase Center. *Biochemistry 49*, 1160−1175.
(17) Yao, H., Jepkorir, G., Lovell, S., Nama, P. V., Weeratunga, S., Battaile, K. P., and Rivera, M. (2011) Two distinct ferritin-like molecules in *Pseudomonas aeruginosa*: The product of the bfrA gene is a bacterial ferritin (FtnA) and not a bacterioferritin (Bfr). *Biochemistry 50*, 5236−5248.
(18) Macedo, S., Romão, C. V., Mitchell, E., Matias, P. M., Liu, M. Y., Xavier, A. V., LeGall, J., Teixeira, M., Lindley, P., and Carrondo, M. A. (2003) The Nature of the Di-Iron Site in the Bacterioferritin from *Desulfovibrio desulfuricans*. *Nat. Struct. Biol. 10*, 285−290.
(19) Takahashi, T., and Kuyucak, S. (2003) Functional properties of three-fold and four-fold channels in ferritin deduced from electrostatic calculations. *Biophys. J. 84*, 2256−2263.
(20) Liu, H.-L., Zhou, H.-N., Xing, W.-M., Zhao, J.-F., Li, S.-X., Huang, J.-F., and Bi, R.-C. (2004) 2.6 Å Resolution Crystal Structure of the Bacterioferritin from *Azotobacter vinelandii*. *FEBS Lett. 573*, 93−98.
(21) Swartz, L., Kuchinskas, M., Li, H., Poulos, T. L., and Lanzilotta, W. N. (2006) Redox-dependent structural changes in the *Azotobacter vinelandii* bacterioferritin: New insights into the ferroxidase and iron transport mechanism. *Biochemistry 45*, 4421−4428.
(22) Yao, H., Wang, Y., Lovell, S., Kumar, R., Ruvinsky, A. M., Battaile, K. P., Vakser, I. A., and Rivera, M. (2012) The Structure of the BfrB-Bfd Complex Reveals Protein-Protein Interactions Enabling Iron Release from Bacterioferritin. *J. Am. Chem. Soc. 134*, 13470−13481.
(23) Jo, S., Kim, T., Iyer, V. G., and Im, W. (2008) CHARMM-GUI: A web-based graphical user interface for CHARMM. *J. Comput. Chem. 29*, 1859−1865.
(24) Brooks, B. R., Brooks, C. L., III, MacKerell, A. D., Jr., Nilsson, L., Petrella, R. J., Roux, B., Won, Y., Archontis, G., Bartels, C., Boresch, S., Caflisch, A., Caves, L., Cui, Q., Dinner, A. R., Feig, M., Fischer, S., Gao, J., Hodoscek, M., Im, W., Kuczera, K., Lazaridis, T., Ma, J., Ovchinnikov, V., Paci, E., Pastor, R. W., Post, C. B., Pu, J. Z., Schaefer, M., Tidor, B., Venable, R. M., Woodcock, H. L., Wu, X., Yang, W., York, D. M., and Karplus, M. (2009) CHARMM: The Biomolecular Simulation Program. *J. Comput. Chem. 30*, 1545−1614.
(25) Lee, K. I., Jo, S., Rui, H., Egwolf, B., Roux, B., Pastor, R. W., and Im, W. (2012) Web interface for Brownian dynamics simulation of ion transport and its applications to β-barrel pores. *J. Comput. Chem. 33*, 331−339.
(26) Im, W., and Roux, B. (2002) Ion permeation and selectivity of OmpF porin: A theoretical study based on molecular dynamics, Brownian dynamics, and continuum electrodiffusion theory. *J. Mol. Biol. 322*, 851−869.
(27) Ermak, D. L., and Mccammon, J. A. (1978) Brownian Dynamics with Hydrodynamic Interactions. *J. Chem. Phys. 69*, 1352−1360.
(28) Chandrasekhar, S. (1943) Stochastic problems in physics and astronomy. *Rev. Mod. Phys. 15*, 0001−0089.
(29) Phillips, J. C., Braun, R., Wang, W., Gumbart, J., Tajkhorshid, E., Villa, E., Chipot, C., Skeel, R. D., Kale, L., and Schulten, K. (2005) Scalable molecular dynamics with NAMD. *J. Comput. Chem. 26*, 1781−1802.
(30) MacKerell, A. D., Bashford, D., Bellott, M., Dunbrack, R. L., Evanseck, J. D., Field, M. J., Fischer, S., Gao, J., Guo, H., Ha, S., Joseph-McCarthy, D., Kuchnir, L., Kuczera, K., Lau, F. T. K., Mattos, C., Michnick, S., Ngo, T., Nguyen, D. T., Prodhom, B., Reiher, W. E., Roux, B., Schlenkrich, M., Smith, J. C., Stote, R., Straub, J., Watanabe, M., Wiorkiewicz-Kuczera, J., Yin, D., and Karplus, M. (1998) All-atom empirical potential for molecular modeling and dynamics studies of proteins. *J. Phys. Chem. B 102*, 3586−3616.
(31) Mackerell, A. D., Feig, M., and Brooks, C. L. (2004) Extending the treatment of backbone energetics in protein force fields: Limitations of gas-phase quantum mechanics in reproducing protein conformational distributions in molecular dynamics simulations. *J. Comput. Chem. 25*, 1400−1415.
(32) Durell, S. R., Brooks, B. R., and Benniam, A. (1994) Solvent-induced forces between two hydrophillic groups. *J. Phys. Chem. 98*, 2198−2202.
(33) Steinbach, P. J., and Brooks, B. R. (1994) New Spherical-Cutoff Methods for Long-Range Forces in Macromolecular Simulation. *J. Comput. Chem. 15*, 667−683.
(34) Shannon, R. (1976) Revised effective ionic radii and systematic studies of interatomic distances in halides and chalcogenides. *Acta Crystallogr. A32*, 751−767.
(35) Le Brun, N. E., Wilson, M. T., Andrews, S. C., Guest, J. R., Harrison, P. M., Thomson, A. J., and Moore, G. R. (1993) Kinetic and structural characterization of an intermediate in the biomineralization of bacterioferritin. *FEBS Lett. 333*, 197−202.
(36) Weeratunga, S. K., Gee, C. E., Lovell, S., Zeng, Y., Woodin, C. L., and Rivera, M. (2009) Binding of *Pseudomonas aeruginosa* apobacterioferritin-associated ferredoxin to bacterioferritin B promotes heme mediation of electron delivery and mobilization of core mineral iron. *Biochemistry 48*, 7420−7431.
(37) DeLano, W. L. (2002) *The PyMOL Molecular Graphics System*, DeLano Scientific, San Carlos, CA.